PTEP

Prog. Theor. Exp. Phys. **2015**, 073G01 (16 pages)
DOI: 10.1093/ptep/ptv088

Magnetic field enhancement at a pit on the surface of a superconducting accelerating cavity

Takayuki Kubo*

KEK, High Energy Accelerator Research Organization, 1-1 Oho, Tsukuba, Ibaraki 305-0801, Japan
*E-mail: kubotaka@post.kek.jp

Received March 30, 2015; Revised May 18, 2015; Accepted May 27, 2015; Published July 6, 2015

The thermal magnetic breakdown due to the magnetic field enhancement at a pit is the major obstacle to achieving a high accelerating field using a superconducting radio-frequency cavity. The well-type pit model has attracted attention as a model of the magnetic field enhancement at a pit, whose enhancement factor depends only on an edge radius normalized by the pit width. However, many of the pits found on cavity surfaces are not well type but have gentle slopes, and the impacts of the slope angle on the enhancement factor have not yet been well understood. In the present study, we introduce a model that can describe a pit with an arbitrary slope angle and evaluate its enhancement factor. A two-dimensional model is enough to describe the magnetic field enhancement at the pit. To evaluate the enhancement factor, an analytical method based on the conformal mapping was developed. The results are compared with those obtained by a simulation method, developed in this paper, that utilizes two-dimensional "electrostatics." A general formula to evaluate the enhancement factor was derived, which agreed well with the simulation results. We found that not only the normalized edge radius but also the slope angle had a substantial impact on the enhancement factor. A pit with a gentle slope angle yields a much smaller enhancement factor than a well-type pit. The results can be applied to the calculation of the enhancement factors of real pits with arbitrary slope angles.

Subject Index G05

1. Introduction

The superconducting (SC) radio-frequency (RF) cavity has been developed as one of the core components of modern particle accelerators [1]. Improvements in cavity fabrication technologies have significantly pushed up the accelerating field, E_{acc}, over the last few decades [2]. Some TESLA-shape nine-cell cavities made of pure niobium have achieved $E_{\mathrm{acc}} > 45\,\mathrm{MV\,m^{-1}}$ [3], which is close to the fundamental limit of the niobium cavity in terms of the surface magnetic field [4]. Such a high field, however, cannot regularly be achieved due to thermal magnetic breakdown, so-called quench, triggered by normal-metal contaminants or geometrical defects. At present, the possibilities of involving metallic contaminants during fabrication processes are thought to be significantly reduced by modern surface preparation processes, i.e., electropolishing [5,6], high-pressure rinsing [7–9], and clean assembly [10]. On the other hand, a geometrical defect such as a pit accompanying electron-beam welding remains as one of the major concerns even today [11]. An example of a quench-inducing pit is shown in Fig. 1 (see also Refs. [11–15]).

The magnetic field enhancement (MFE) effect is the key to understanding the quench due to a pit. The surface magnetic field in the vicinity of a pit is generally written as

$$H(\mathbf{r}) = \beta(\mathbf{r})H_0, \quad 0 \le \beta(\mathbf{r}) \le \beta_{\mathrm{M}}, \tag{1}$$

© The Author(s) 2015. Published by Oxford University Press on behalf of the Physical Society of Japan.
This is an Open Access article distributed under the terms of the Creative Commons Attribution License (http://creativecommons.org/licenses/by/4.0/), which permits unrestricted reuse, distribution, and reproduction in any medium, provided the original work is properly cited.

Downloaded from http://ptep.oxfordjournals.org/ at CERN Library on July 9, 2015

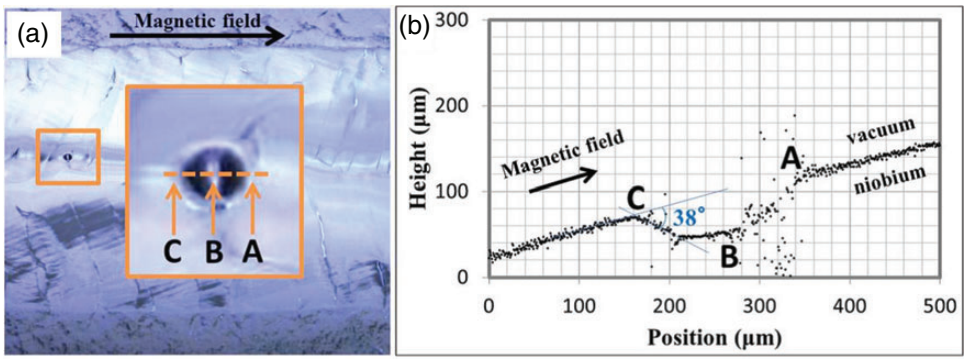

Fig. 1. A quench-inducing pit found on an equator weld of a cavity [15]. The cavity performance was limited by a quench at $E_{\mathrm{acc}} = 31\,\mathrm{MV\,m^{-1}}$. (a) An optical image taken by the Kyoto camera [11]. (b) A profile of the replica extracted by laser microscopy.

where $\mathbf{r}$ is a position, H_0 is the surface magnetic field far from the pit, and $\beta(\mathbf{r})$ is a coefficient introduced to reflect the effect of the pit geometry. $\beta(\mathbf{r})$ reaches its maximum value, β_{M}, at the edge [16–20]. If the enhanced field, $\beta_{\mathrm{M}} H_0$, is large enough, the edge becomes normal conducting due to thermal and magnetic effects, which triggers a thermal runaway [21,22]. A difference of edge shape affects the β_{M} factor and thus the breakdown field. To reveal the relation between the β_{M} factor and the geometry of the pit is the first step to understanding the quench due to the pit.

An important contribution to understanding the MFE at a pit was made by Shemelin and Padamsee [19]. They numerically studied the β_{M} factor of the "well-type" pit and proposed a simple relation, $\beta_{\mathrm{M}} \propto (r_e/R)^{-\frac{1}{3}}$, where r_e is the radius of the edge and R is half the well width. Their result enabled quantitative discussions on the MFE at a pit and furthermore opened the way to evaluating β_{M} for pits with only the two measurable parameters, r_e and R, which was then used for evaluating β_{M} of well-type artificial pits in experimental studies [22]. However, many of the pits found on cavity surfaces are not well type but have gentle slopes, as shown in Fig. 1, where the slope angle is 38°. It is not clear whether discussions based on the well-type pit model are applicable to such a pit with gentle slopes. The impact of the slope angle on the β_{M} factor have not been well understood.

The present study aims to qualitatively and quantitatively understand the MFE at a pit with any slope angle. We introduce a model that can describe a pit with an arbitrary slope angle. To evaluate its β_{M} factor, an analytical method and a simulation method were developed. By using these methods, the β_{M} factor of the model was evaluated. An extremely useful formula for the evaluation of the β_{M} factor was derived, which agreed well with the simulation results. Based on the results, we discuss the impact of the slope angle on the β_{M} factor and an application of the model to real pits.

2. Model and formulations

2.1. Model

A typical wavelength of an SCRF cavity, $\mathcal{O}(10^{-1})\,\mathrm{m}$, is much larger than the size of pits, $\mathcal{O}(10^{-5}$–$10^{-4})\,\mathrm{m}$; the RF wavelength can be regarded as infinity. Thus, in the following, we study a model in the framework of magnetostatics.

The magnetic field is enhanced at edges perpendicular to the direction of the surface magnetic field [19–22], which correspond to A and C in Fig. 1. The detailed shapes of other parts of the edges are not essential. Thus the MFE of a pit is well approximated by a groove perpendicular to the direction of the surface magnetic field. In fact, the β_{M} factor of a three-dimensional well-type pit

Downloaded from http://ptep.oxfordjournals.org/ at CERN Library on July 9, 2015

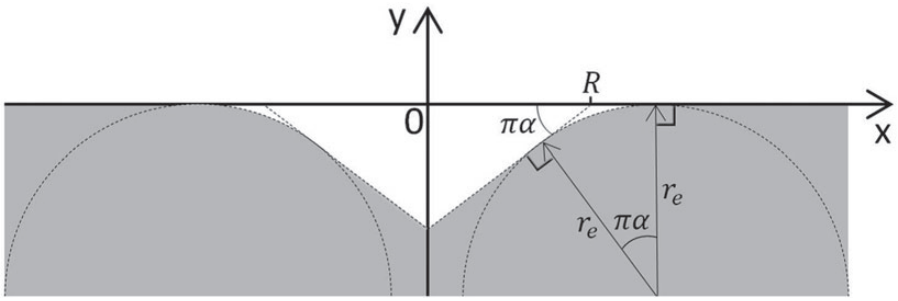

Fig. 2. Model of pit. Gray and white regions represent the SC in the Meissner state and the vacuum, respectively. r_e is the radius of the edge, R is half the width of the pit aperture, and $\pi\alpha$ $(0 < \alpha < 1/2)$ is the slope angle. The arcs of the edges are smoothly connected to the slopes and the flat surfaces.

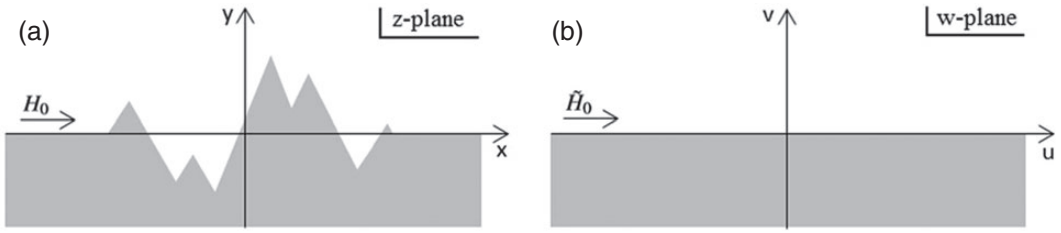

Fig. 3. General two-dimensional irregularity, (a) on the z-plane, and (b) its map on the w-plane.

has the same functional form as the two-dimensional one, as shown in the previous studies [19,22]. Furthermore, since the magnetic field attenuates toward the bottom [19–22], the bottom shape is not essential for describing the MFE. We developed the two-dimensional model shown in Fig. 2. Its geometry is parametrized by r_e, R, and α, where r_e is the radius of the edge, R is half the width of the pit aperture, and $\pi\alpha$ $(0 < \alpha < 1/2)$ is the slope angle. Note that a pit with $\alpha \to 1/2$ corresponds to a well-type pit with an infinite depth.

2.2. Formulation for analytical evaluations

Let us formulate the MFE in the vicinity of a general two-dimensional irregularity [see Fig. 3(a)]. The Maxwell equations for two-dimensional magnetostatics in the vacuum are given by $\mathrm{rot}\,\mathbf{H} = \mathbf{0}$ and $\mathrm{div}\,\mathbf{B} = 0$, where $\mathbf{H}$ is a magnetic field, $\mathbf{B} = \mu_0\mathbf{H}$ is a magnetic flux density, and μ_0 is the magnetic permeability of the vacuum. By introducing a magnetic scalar potential $\phi(x, y)$, the problem is reduced to a Laplace equation, $\triangle^{(2)}\phi(x, y) = 0$, where $\triangle^{(2)} \equiv \partial^2/\partial x^2 + \partial^2/\partial y^2$. Then the magnetic field is given by $\mathbf{H} = -\mathrm{grad}\,\phi = (-\partial\phi/\partial x, -\partial\phi/\partial y, 0)$. On the other hand, by introducing a vector potential $\mathbf{A} = (0, 0, -\mu_0\,\psi(x, y))$, where ψ is a real function, the problem is reduced to the Laplace equation $\triangle^{(2)}\psi(x, y) = 0$. The magnetic field is given by $\mathbf{H} = \mu_0^{-1}\,\mathrm{rot}\,\mathbf{A} = (-\partial\psi/\partial y, \partial\psi/\partial x, 0)$. Since both approaches should lead to the same magnetic field, we find

$$H_x = -\frac{\partial\phi}{\partial x} = -\frac{\partial\psi}{\partial y}, \quad H_y = -\frac{\partial\phi}{\partial y} = \frac{\partial\psi}{\partial x}, \tag{2}$$

which are the Cauchy–Riemann conditions. Thus a function defined by

$$\Phi(z) \equiv \phi(x, y) + i\psi(x, y) \tag{3}$$

Downloaded from http://ptep.oxfordjournals.org/ at CERN Library on July 9, 2015

is an holomorphic function of $z = x + iy$, called the complex potential. When $\Phi(z)$ is given, the components of the magnetic field are derived from

$$H_x - iH_y = -\frac{\partial\phi}{\partial x} + i\frac{\partial\phi}{\partial y} = -\frac{\partial\phi}{\partial x} - i\frac{\partial\psi}{\partial x} = -\frac{d\Phi(z)}{dz}, \tag{4}$$

where the property of the holomorphic function that $d\Phi(z)/dz = \partial\phi/\partial x + i\partial\psi/\partial x$ is used. Thus the two-dimensional magnetostatics problem is reduced to the problem of finding $\Phi(z)$.

The complex potential $\Phi(z)$ can be derived from a complex potential $\widetilde{\Phi}(w)$ on the w-plane with a flat surface [see Fig. 3(b)] that is connected to the physical z-plane with a conformal mapping, $z = F(w)$. The map is given by the Schwarz–Christoffel transformation [23],

$$z = F(w) = P\int_0^w f(w)dw + Q, \tag{5}$$

where $f(w)$ is a function on the w-plane, and P and Q are constants. Here we introduce a complex potential on the w-plane, $\widetilde{\Phi}(w) = -\widetilde{H}_0 w$ with $\widetilde{H}_0 \equiv PH_0$, which reproduces the uniform magnetic-field on the w-plane, $H_u - iH_v = -\widetilde{\Phi}'(w) = \widetilde{H}_0$. Then the complex potential on the z-plane is given by

$$\Phi(z) = \widetilde{\Phi}(F^{-1}(z)) = -\widetilde{H}_0 F^{-1}(z), \tag{6}$$

where F^{-1} is the inverse function of F. By using Eqs. (4)–(6), we find

$$\beta(x, y) \equiv \frac{|\mathbf{H}(x, y)|}{H_0} = \frac{|H_x - iH_y|}{H_0} = \frac{|\Phi'(z)|}{H_0} = \frac{\widetilde{H}_0}{H_0}\left|\frac{dF^{-1}(z)}{dz}\right| = \left|\frac{1}{f(w)}\right|_{w=F^{-1}(z)}, \tag{7}$$

where $dF^{-1}/dz = dw/dz = (dz/dw)^{-1} = (dF/dw)^{-1}$ is used. The β_{M} factor is calculated by the maximum value of $\beta(x, y)$. In principle, the β_{M} factor of any two-dimensional irregularity can be evaluated by using Eq. (7), if an explicit form of the Schwarz–Christoffel transformation and its inverse are known.

2.3. *Simulation method*

A simulation code for the "electrostatic" problem is useful to evaluate the β_{M} factor of our model, because the β_{M} factor of a two-dimensional irregularity on an SC is equivalent to the electric field enhancement factor (β_{E} factor) of the same irregularity on a conductor. Let us consider Fig. 3 again. This time, we regard the gray and white regions as the conductor and the vacuum, respectively, and replace the magnetic field far from the irregularity $\mathbf{H} = (H_0, 0)$ by the electric field $\mathbf{E} = (0, -E_0)$. In much the same way as the magnetostatics problem, the electrostatics problem on the xy-plane is also reduced to the problem of finding a holomorphic complex potential on the z-plane, $\Phi_E(z)$ [24, 25]. The components of the electric field are given by

$$E_x - iE_y = -\frac{d\Phi_E(z)}{dz}. \tag{8}$$

The complex potential $\Phi_E(z)$ can be derived from a complex potential $\widetilde{\Phi}_E(w)$ on the w-plane with a flat surface that is connected to the physical z-plane with a conformal mapping given by Eq. (5). We introduce a complex potential on the w-plane, $\widetilde{\Phi}_E(w) = -i\widetilde{E}_0 w$ with $\widetilde{E}_0 \equiv PE_0$, which reproduces the uniform electric field on the w-plane; $E_u - iE_v = -\widetilde{\Phi}'_E(w) = i\widetilde{E}_0$ or $(E_u, E_v) = (0, -\widetilde{E}_0)$.

Downloaded from http://ptep.oxfordjournals.org/ at CERN Library on July 9, 2015

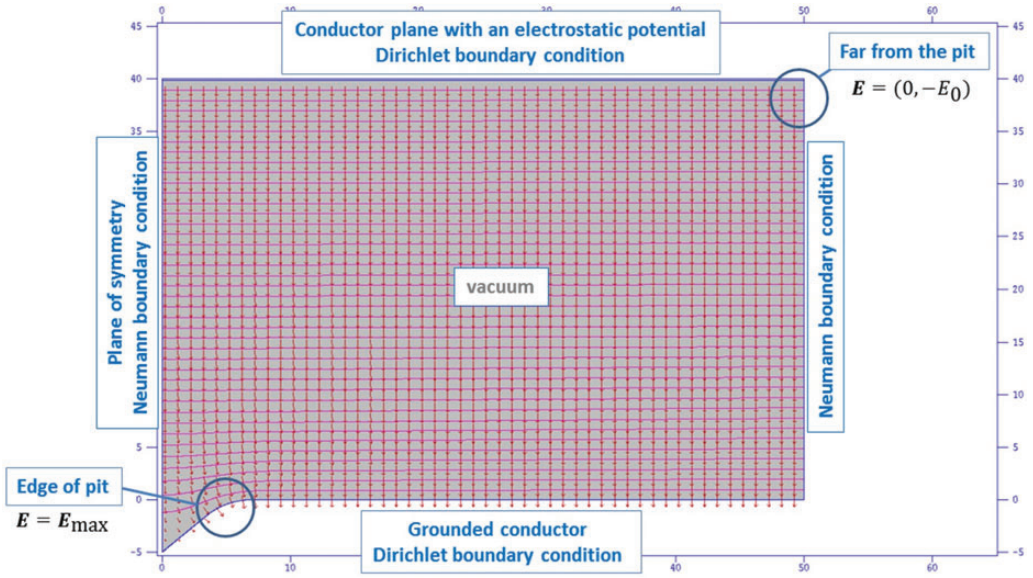

Fig. 4. Simulation domain on POISSON, which corresponds to the right half of Fig. 2. A pit is located at the lower left. The left boundary corresponds to the plane of symmetry. The upper and lower boundaries correspond to conductors with different electrostatic potentials, which generate an electric field distribution. Equipotential lines and arrows representing electric field vectors are also shown. The electric field is uniform far from the pit; $\mathbf{E} = (0, -E_0)$. On the other hand, the electric field is enhanced and reaches its maximum near the edge; $\mathbf{E} = \mathbf{E}_{\max}$. The β_{E} factor is given by $|\mathbf{E}_{\max}|/E_0$.

Then the complex potential on the z-plane is given by

$$\Phi_E(z) = \widetilde{\Phi}_E\left(F^{-1}(z)\right) = -i\widetilde{E}_0 F^{-1}(z). \tag{9}$$

By using Eqs. (8) and (9), we find

$$\beta(x, y) \equiv \frac{|\mathbf{E}(x, y)|}{E_0} = \frac{|E_x - iE_y|}{E_0} = \left|\frac{1}{f(w)}\right|_{w=F^{-1}(z)}, \tag{10}$$

which completely corresponds with that of the magnetic field. Then we find

$$\beta_{\mathrm{M}} = \beta_{\mathrm{E}}. \tag{11}$$

Thus the β_{M} factor can generally be evaluated by calculating the β_{E} factor of the same irregularity.

We use POISSON, a two-dimensional electrostatic simulation code [26–28]. Figure 4 shows an example simulation domain, which corresponds to the right half of Fig. 2. The left boundary corresponds to the plane of symmetry. The lower conductor has a pit with a geometry parametrized by α, r_e, and R. Another conductor plane is located at the upper boundary. The difference of electrostatic potentials between the upper and lower conductors yields an electric field, which is uniform, $\mathbf{E} = (0, -E_0)$, far from the pit. In the vicinity of the edge of pit, the electric field is enhanced and reaches its maximum value, $\mathbf{E} = \mathbf{E}_{\max}$. Then the β_{E} factor is given by $|\mathbf{E}_{\max}|/E_0$, and we find

$$\beta_{\mathrm{M}} = \beta_{\mathrm{E}} = \frac{|\mathbf{E}_{\max}|}{E_0}, \tag{12}$$

where Eq. (11) is used. In an implementation of the simulation, we must pay attention to locating the positions of the right and upper boundaries well away from the pit and adopting a fine-enough mesh near the pit. Otherwise, the simulation results depend largely on these parameters. We placed the right and upper boundaries at $x = 10\mathrm{R}$ and $y = 8\mathrm{R}$, respectively, which are far enough away from the pit. The mesh size was set at $0.003\mathrm{R}$ ($< 10^{-2}\mathrm{R}$), which is small enough for the evaluation of

Downloaded from http://ptep.oxfordjournals.org/ at CERN Library on July 9, 2015

the model with an edge radius $r_e > \mathcal{O}(10^{-1})$R. For the evaluation of the model with $r_e < 10^{-1}$R, a simulation with smaller meshes is preferred.

3. Evaluation of the β_{M} factor of the model

3.1. Sharp-edge model

Let us begin with a sharp-edge model as shown in Fig. 5, which can be regarded as the limit, $r_e/R \to 0$, of the original model. This simplified model is not only an instructive exercise of the formulation developed in the last section, but also a rough sketch that provides us with a rudimentary understanding of the MFE at the pit [29,30].

The mapping that connects the physical z-plane [Fig. 5(a)] to the w-plane [Fig. 5(b)] is given by Eq. (5) with $f(w) = f_0(w)$ [23], where

$$f_0(w) = \left(w^2 - 1\right)^{\alpha} w^{-2\alpha}. \tag{13}$$

Constants $P = p_0 R$ and $Q = q_0 R$ are obtained by imposing the conditions that A′ and B′ on the w-plane are mapped into A and B on the z-plane, respectively (see Appendix A):

$$p_0 = \frac{\sqrt{\pi}}{\alpha \cos \pi\alpha \, \Gamma(\alpha)\Gamma\left(\frac{1}{2} - \alpha\right)}, \tag{14}$$

$$q_0 = -i \tan \pi\alpha. \tag{15}$$

Then $\beta(x, y)$ can be evaluated by using the general formula, Eq. (7):

$$\beta(x, y) = \left|\frac{1}{f_0(w)}\right|_{w=F^{-1}(z)} = \left|\frac{w^{2\alpha}}{\left(w^2 - 1\right)^{\alpha}}\right|_{w=F^{-1}(z)}. \tag{16}$$

Note that $\beta(\infty) = \beta|_{w\to\infty} = 1$, which is consistent with the fact that the magnetic field is not enhanced far away from the pit. By using Eq. (16), β at A and B are immediately obtained:

$$\beta(\mathrm{A}) = \beta|_{w=1} = \infty, \tag{17}$$

$$\beta(\mathrm{B}) = \beta|_{w=0} = 0. \tag{18}$$

The magnetic field is enhanced at the edge and vanishes at the bottom. These behaviors qualitatively correspond with the observations so far [19–22].

In order to evaluate β at an arbitrary $z = x + iy$, an explicit form of $f_0(F^{-1}(z))$ is required [see Eq. (16)]. This task is approximately achieved by focusing on a small region around an edge [24,25]. Let us look at the vicinity of the edge A, which corresponds to the vicinity of A′ on the w-plane, $w = 1 + \epsilon$ ($|\epsilon| \ll 1$). Then $f_0(w)$ can be approximated by $f_0(w) \simeq 2^{\alpha}\epsilon^{\alpha}$, and Eq. (5) is calculated as $z = R + 2^{\alpha} p_0 R \epsilon^{\alpha+1}/(\alpha + 1)$. Thus we find $\epsilon^{\alpha+1} = (\alpha + 1)(z - R)/\left(2^{\alpha} p_0 R\right)$ and $f_0(w) \simeq 2^{\alpha}\epsilon^{\alpha} = [2(\alpha + 1)(z - R)/(p_0 R)]^{\alpha/(1+\alpha)}$. Then Eq. (16) becomes

$$\beta(x, y) = \left[\frac{p_0}{2(1 + \alpha)} \frac{R}{r}\right]^{\frac{\alpha}{1+\alpha}}, \tag{19}$$

where $r \equiv |z - R| = \sqrt{(x - R)^2 + y^2}$ is the distance from the edge A. By using Eq. (19), we can evaluate β for arbitrary (x, y) near the edge, in the range given by $|\epsilon| \ll 1$ or $r \ll 2^{\alpha} p_0 R/(1 + \alpha)$.

The round-edge model shown in Fig. 2, which we call the original model, can also be described by the sharp-edge model at some level. The original model has the same geometry as the sharp-edge model except for the arcs: the geometry of the outside of the arcs of the original model corresponds

Downloaded from http://ptep.oxfordjournals.org/ at CERN Library on July 9, 2015

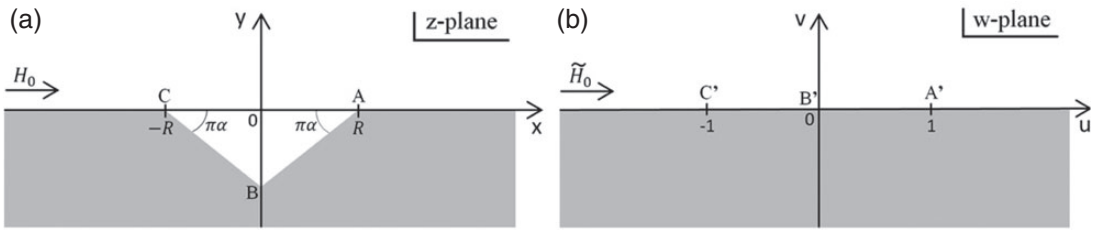

Fig. 5. Sharp-edge model for a rough evaluation. (a) Pit with sharp edges on the z-plane; (b) its map on the w-plane. Gray and white regions represent the SC in the Meissner state and the vacuum, respectively.

with that of the sharp-edge model at $r > r_\Lambda \equiv r_e(1-\cos\pi\alpha)/\sin\pi\alpha$ [29]. Thus the surface magnetic field and β at the outside of the arcs of the original model should be approximated by those of the sharp-edge model at $r > r_\Lambda$. Then β at the boundary of the arc and the flat surface can be evaluated by substituting $r = r_\Lambda$ into Eq. (19), which is expected to be a rough estimate of the $\beta_{\rm M}$ factor when r_e/R is small:

$$\beta_{\rm M} \sim \left(\frac{r_e}{R}\right)^{-\frac{\alpha}{1+\alpha}}. \tag{20}$$

In the following, we evaluate the original model with a finite r_e/R, where we found the relation Eq. (20) is reproduced at the sharp-edge limit, $r_e/R \to 0$.

3.2. *Round-edge model*

For a quantitative evaluation of the $\beta_{\rm M}$ factor of the original model, the edge radius must be explicitly taken into account. An infinite number of triangles can express the arc of the round edge, as shown in Fig. 6. This approach can be regarded as the generalized version of the chamfered-edge model studied by the author [30]. The mapping that connects the physical z-plane [Fig. 6(a)] to the w-plane [Fig. 6(b)] is given by Eq. (5) with $f(w) = \lim_{n\to\infty} f_n(w)$ [23], where

$$f_n(w) = \left(w^2 - w_n^2\right)^{\frac{\alpha}{2n}} \left(w^2-1\right)^{\frac{\alpha}{2n}} w^{-2\alpha} \prod_{k=1}^{n-1} \left(w^2 - w_k^2\right)^{\frac{\alpha}{n}}, \tag{21}$$

and

$$w_k = \begin{cases} 1 + 2\dfrac{\Delta}{n-2} & (k=1), \\ 1 + (k+1)\dfrac{\Delta}{n-2} & (2 \le k \le n-1), \\ 1 + (n+2)\dfrac{\Delta}{n-2} & (k=n). \end{cases} \tag{22}$$

The constants $Q = qR$, $P = pR$, and Δ are determined by the conditions that B$'$, A$_1'$, and A$_0'$ on the w-plane are mapped onto B, A$_1$, and A$_0$ on the z-plane (see Appendix B). The first condition yields

$$q = -i\tan\pi\alpha. \tag{23}$$

The second and the third conditions are somewhat complicated, but, under the assumption $\Delta \ll 1$ (see Appendix B), they are reduced to

$$\Delta^{1+\alpha} p = \frac{\pi\alpha e^\alpha}{2^\alpha}\frac{r_e}{R}, \tag{24}$$

$$(1+\alpha\Delta)p = \frac{1-2\alpha}{{}_2F_1(a,b;c;\zeta)}\left(\frac{1}{\cos\pi\alpha} - \frac{r_e}{R}\frac{1-\cos\pi\alpha}{\sin\pi\alpha}\right), \tag{25}$$

Downloaded from http://ptep.oxfordjournals.org/ at CERN Library on July 9, 2015

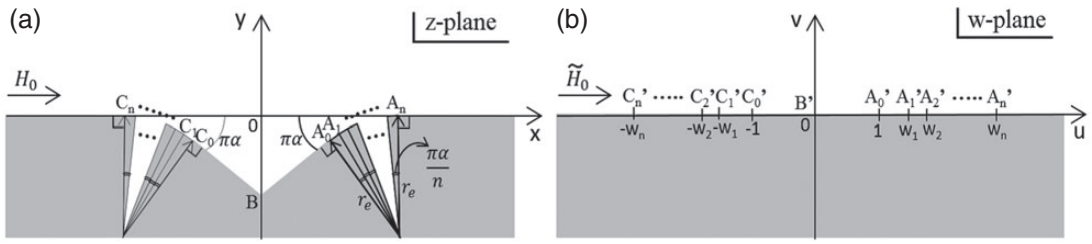

Fig. 6. (a) The model on the z-plane, and (b) its map on the w-plane. The arcs of the edges are expressed by an infinite number of triangles. The gray and white regions represent the SC in the Meissner state and the vacuum, respectively.

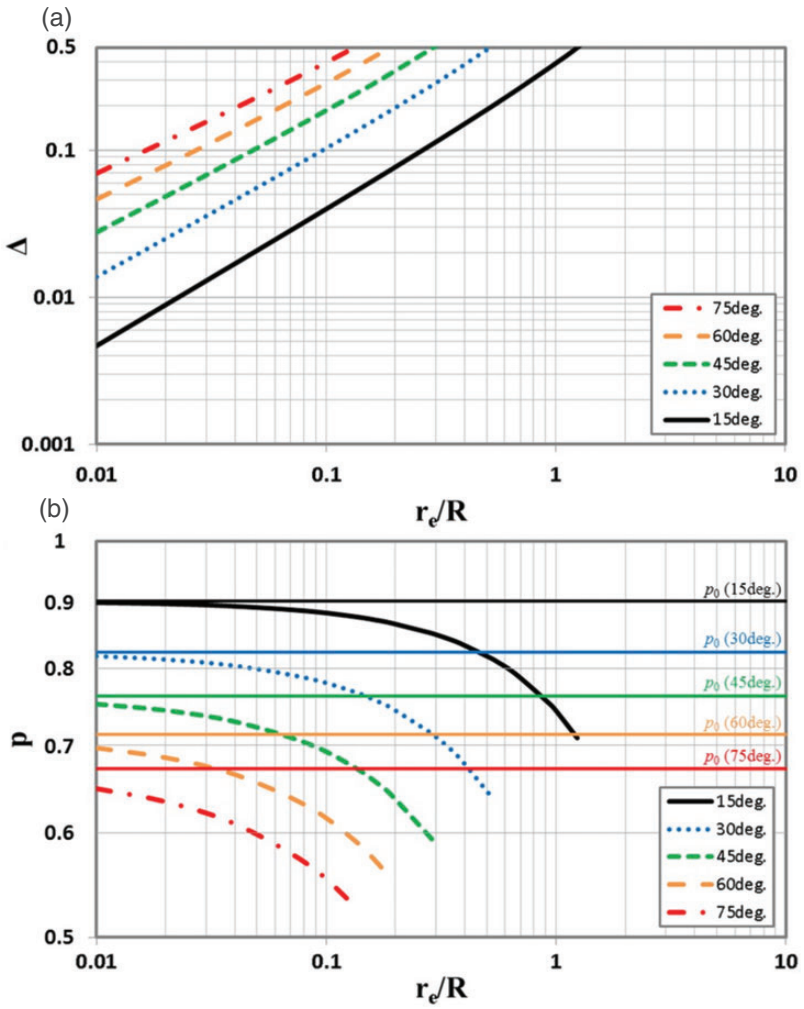

Fig. 7. (a) Δ and (b) p as functions of r_e/R, as given by solutions of Eqs. (24) and (25). p_0 given by Eq. (14) is also shown for comparison.

where ${}_2F_1(a, b; c; \zeta)$ is the Gaussian hypergeometric function with $a \equiv -\alpha$, $b \equiv 1/2 - \alpha$, $c \equiv 1 + b$, and $\zeta \equiv 1 - \Delta$. Then Δ and p are obtained by solving Eqs. (24) and (25) in a self-consistent manner. Figure 7 shows Δ and p as functions of r_e/R.

Here we check that the mapping defined by Eqs. (21)–(25) reproduces that of the sharp-edge model in the limit $r_e/R \to 0$. Equation (23) shows that q equals q_0 independently of

Downloaded from http://ptep.oxfordjournals.org/ at CERN Library on July 9, 2015

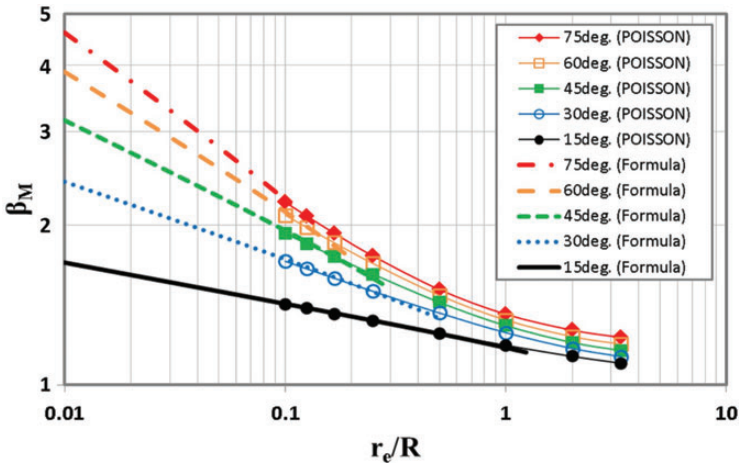

Fig. 8. β_M factors evaluated by using the formula Eq. (26), and those obtained by the simulation code POISSON, are shown as functions of r_e/R for slope angles 15°, 30°, 45°, 60°, and 75°. In view of the self-consistency condition, $\Delta \ll 1$, only r_e/R corresponding to $\Delta < 0.5$ are shown as results of the formula [see also Fig. 7(a)]. The symbols at $(r_e/R)^{-1} = 0.3, 0.5, 1, 2, 4, 6, 8, 10$ correspond to simulation results.

r_e/R. Since $p \neq 0$, Eq. (24) yields $\Delta \to 0$ at $r_e/R \to 0$, which is shown in Fig. 7(a). Then Eq. (22) is reduced to $w_k \to 1$ $(k = 1, \ldots, n)$, and Eq. (21) is reduced to $f_n(w) \to f_0(w)$. Since $c = 1 + b$ and $\zeta = (1 - \Delta) \to 1$, we obtain ${}_2F_1(a, b; c; \zeta) \to \Gamma(1 - a)\Gamma(1 + b)/\Gamma(1 - a + b) = (1 - 2\alpha)\Gamma(1 + \alpha)\Gamma(1/2 - \alpha)/\sqrt{2}$. Then Eq. (25) yields $p \to p_0$, which is shown in Fig. 7(b). Thus, when $r_e/R \to 0$, $f_n(w) \to f_0(w)$, $p \to p_0$, and $q = q_0$, which shows that the mapping is reduced to the sharp-edge model.

The MFE is expected to reach its maximum near the tip of the edge, which corresponds to $w \simeq w_M \equiv (1 + w_n)/2$ on the w-plane. Then the β_M factor is approximated by $\beta_M \simeq \lim_{n\to\infty} |1/f_n(w_M)|$. After some calculations (see Appendix C), we find

$$\beta_M \simeq e^{\alpha}\Delta^{-\alpha} = \left(\frac{e}{\pi}\frac{2^{\alpha}}{\alpha}p\right)^{\frac{\alpha}{1+\alpha}} \left(\frac{r_e}{R}\right)^{-\frac{\alpha}{1+\alpha}}, \tag{26}$$

where Eq. (24) is used. Figure 8 shows β_M calculated by Eq. (26) as functions of r_e/R. At the sharp-edge limit, $r_e/R \to 0$, as is obvious from Eq. (26), $\log_{10}\beta_M$ is a linear function of $\log_{10}(r_e/R)$ with a negative slope $-\alpha/(1 + \alpha)$; the result of the sharp-edge model, Eq. (20), is reproduced. As r_e/R increases, β_M continues decreasing, but the linearity of $\log_{10}\beta_M$ is gradually lost due to the r_e/R dependence of p [see Fig. 7(b)]. As r_e/R further increases, the formula ceases to be applicable. Not only the assumption $\Delta \ll 1$, but also the postulate that β_M reaches its maximum in the vicinity of w_M are not valid in these regions, where the analytical approach is not applicable.

3.3. *Simulation of round-edge geometry*

Simulation results are shown in Fig. 8. Models with slope angles 15°, 30°, 45°, 60°, and 75° and edge radii $(r_e/R)^{-1} = 0.3, 0.5, 1, 2, 4, 6, 8$, and 10 were simulated, which cross the inside and the outside of the range of application of the formula, Eq. (26). In the region of $r_e/R \sim \mathcal{O}(10^{-1})$, the simulation result agrees very well with the analytical calculation. On the other hand, the analytical formula is not applicable in the range $r_e/R \sim \mathcal{O}(1)$, and the β_M factor can only be calculated by simulation, where it remains decreasing as r_e/R increases and reaches $\beta_M \lesssim 1.2$ at $r_e/R \simeq 3$.

Downloaded from http://ptep.oxfordjournals.org/ at CERN Library on July 9, 2015

4. Discussion

As $\alpha \to 1/2$, our model approaches the well-type pit with an infinite depth. By using the formula Eq. (26), we find $\beta_{\mathrm{M}} = 1.16 \times (r_e/R)^{-\frac{1}{3}}$ for $r_e/R \ll 1$, which agrees well with the simulation result of the three-dimensional well-type pit model, $\beta_{\mathrm{M}} = 1.17 \times (r_e/R)^{-\frac{1}{3}}$, by Xie and Liepe [22]. The two-dimensional and three-dimensional models have a good agreement not only in the functional form $\propto (r_e/R)^{-\frac{1}{3}}$ but also in the coefficient. This agreement supports the validity of modeling the pit with the two-dimensional model and shows how effective the formula is. It should be emphasized that the agreement is not surprising; the magnetic field is enhanced at edges perpendicular to the direction of the surface magnetic field, and thus, modeling a cross-section parallel to the direction of the surface magnetic field is enough to describe the MFE, as mentioned in Sect. 2.

Not only the edge radius r_e/R, but also the slope angle $\pi\alpha$ has a substantial impact on β_{M}. This behavior cannot be derived in the framework of the well-type pit model with the fixed slope angle $\pi\alpha = \pi/2$. As shown in Fig. 8, the dependence on the slope angle becomes large at $r_e/R \ll 1$. Let us consider the worst case. As discussed in previous studies [16,19], the effective radius of the edge is limited below by the order of the normal conducting skin depth $\sim$1 μm for RF frequencies of $\mathcal{O}(1)$ GHz. Thus we can set $r_e = 1\,\mu\mathrm{m}$ as the worst case. For a typical pit size, $R \sim 10^2\,\mu\mathrm{m}$, the formula, Eq. (26), is available because $r_e/R \ll 1$. Figure 9 shows β_{M} factors in the worst case as functions of slope angle. The larger the slope angle, the larger the β_{M}. A pit with a slope angle of $\simeq 90^\circ$ and $R = 50\,\mu\mathrm{m}$ can reach $\beta_{\mathrm{M}} > 4$. Pits with the smaller slope angles, however, cannot yield such a large value. For example, when the slope angle is 10°, even in the worst case, $\beta_{\mathrm{M}} = 1.4$–1.5 for $R = 50$–$200\,\mu\mathrm{m}$. The previous study on the well-type pit model by Shemelin and Padamsee [19], which concludes that $\beta_{\mathrm{M}} > 4$ is the worst case for $R = 50\,\mu\mathrm{m}$, is valid only when the slope angle is $\simeq 90^\circ$. Real pits, which have more gentle slopes in general, yield much smaller β_{M} than the well-type pit.

The present model and the results for the β_{M} factor are directly applied for the evaluation of the real pits found on the surface of the cavity. This can be done by extracting the model parameters r_e, R, and $\pi\alpha$ and substituting them into the formula, Eq. (26), or reading from Fig. 8. The parameters can be extracted from a cross-section of the pit parallel to the surface magnetic field obtained by using, for example, laser microscopy combined with the replica technique [14,18,31]. Taking Fig. 1(b) as an example, $R \simeq 1.0 \times 10^2\,\mu\mathrm{m}$ and $\pi\alpha \simeq 0.21\pi$ (38°) are extracted. r_e is given by the minimum value of the curvature radius along the edges. Figure 10 shows the profile and the curvature radius near the edge C, where the curvature radius is calculated by $r_{\mathrm{cur}} = -\left(1 + h'^2\right)^{\frac{3}{2}}/h''$ and $h(x)$, the polynomial corresponding to the fitting curve. Then $r_e = \min[r_{\mathrm{cur}}] \simeq 3.0 \times 10^1\,\mu\mathrm{m}$ is obtained. By using the formula, Eq. (26), we obtain $\beta_{\mathrm{M}} \simeq 1.5$. We should comment on the study by Xie et al. [22], where β_{M} factors of artificially formed pits on the surface of an SCRF cavity were evaluated based on the well-type geometry, and substitute r_e and R extracted from the laser microscopy into their simulation result, $\beta_{\mathrm{M}} = 1.17 \times (r_e/R)^{-\frac{1}{3}}$. As shown in the figures of Ref. [22], however, the profile of the artificial pits is not well type. Actually, it has a slope angle $\simeq 80^\circ$. Thus an application of the well-type pit model might overestimate the β_{M} factor of the artificial pit. Since the dependence on the slope angle becomes significantly large at $r_e/R \ll 1$, the overestimation becomes worse as r_e/R decreases. For example, when $r_e/R = 0.01$, we obtain $\beta_{\mathrm{M}}(80^\circ) = 4.8$ and $\beta_{\mathrm{M}}(89.9^\circ) = 5.3$; the well-type pit model overestimates by 10% in this example.

The viewpoint based on the model formulated in this paper might reduce considerably the time needed for local mechanical grinding [15,31–33]; the grinding removes pits one by one and thus

Downloaded from http://ptep.oxfordjournals.org/ at CERN Library on July 9, 2015

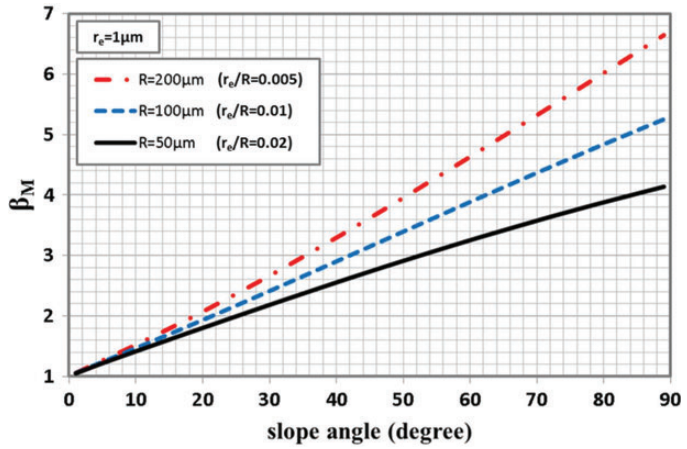

Fig. 9. β_{M} factors in the worst case ($r_e = 1\,\mu\mathrm{m}$) as functions of slope angle. The three curves correspond to $R = 200\,\mu\mathrm{m}$, $100\,\mu\mathrm{m}$, and $50\,\mu\mathrm{m}$, respectively, where the formula, Eq. (26), is available when $r_e/R \ll 1$.

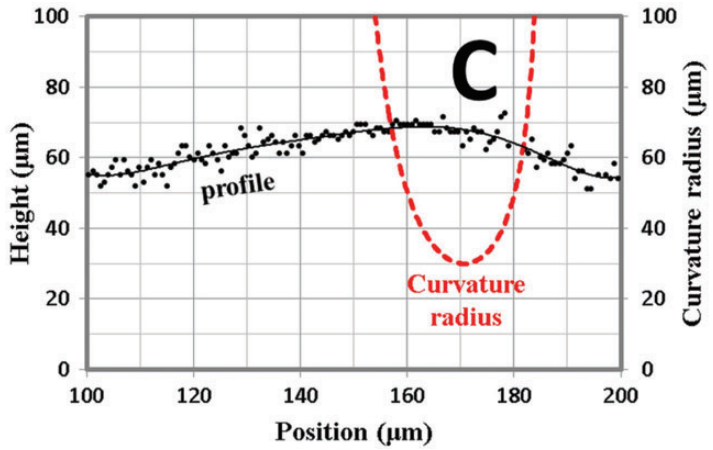

Fig. 10. Profile and curvature radius near the edge C of Fig. 1(b). The solid curve represents the fitting curve of the profile data extracted from laser microscopy. The red dashed curve represents the curvature radius calculated from the fitting curve.

takes a long time if there are many pits. Adopting our model, we can evaluate the β_{M} factors of pits by using experimentally observed model parameters. Then it becomes possible to select only those with large β_{M}. The time required for the curing of the SCRF cavity should be reduced, in particular for the case when a lot of pits with shallow slope angles exist.

It is important to note that the present model and results are applicable not only to pits on current SCRF cavities based on the niobium technology, but also to pits on future SCRF cavities based on new technologies such as a multilayer SC [34,35] or an alternative bulk SC material [36,37]. Furthermore, the present model and results can also be applied to pits on normal conducting cavities, although the motivation of this study originated from one of the challenges that SCRF technology has been facing.

In this paper, the relation between the β_{M} factor and the geometry of a pit is analyzed. This is, however, merely the first step to understanding quenching due to a pit. Thermal calculations taking the magnetic field distribution on the surface into account are the next step.

Downloaded from http://ptep.oxfordjournals.org/ at CERN Library on July 9, 2015

5. Summary

The magnetic field enhancement effect is the key to understanding the thermal magnetic breakdown triggered by a pit. As a model of the magnetic field enhancement at a pit, the well-type pit model had been studied strenuously so far. Real pits found on cavities, however, generally have gentle slopes, as shown in Fig. 1. The magnetic field enhancement at a pit with a realistic slope angle had not been well understood.

A two-dimensional model is enough to describe the magnetic field enhancement at pits, because only the edges perpendicular to the direction of the surface magnetic field are essential for the enhancement. In this paper, we studied a two-dimensional model, shown in Fig. 2, that can describe a pit with an arbitrary slope angle. The pit geometry is parametrized by r_e, R, and $\pi\alpha$, where r_e is the radius of the edge, R is half the width of the pit aperture, and $\pi\alpha$ ($0 < \alpha < 1/2$) is the slope angle. To evaluate the β_{M} factor based on this model, an analytical method was developed based on the conformal mapping. A simulation method that utilizes a simulation code of the "electrostatics" problem was also developed. By using these analytical and simulation methods, the β_{M} factor of a pit with a slope angle was evaluated. An extremely useful formula, Eq. (26), was analytically derived, and it agreed well with the simulation result. The results are summarized in Fig. 8.

We confirmed, at $\alpha \to 1/2$, that the formula reproduces the three-dimensional simulation results for the three-dimensional well-type pit model. This reflects the validity of modeling the pit with a two-dimensional model. Then the impact of the slope angle on the β_{M} factor were discussed, which could not be considered in the framework of the well-type pit model. We found that a pit with a gentle slope angle yielded much smaller β_{M} than that of the well-type pit; a pit with a slope angle $= 10^\circ$ and $R = 50$–$200\,\mu\mathrm{m}$ yields $\beta_{\mathrm{M}} = 1.4$–1.5, even at the worst case. The previous study [19], which concluded that a pit with $R = 50\,\mu\mathrm{m}$ can reach $\beta_{\mathrm{M}} > 4$ at the worst case, is valid only when the pit has a slope angle $\simeq 90^\circ$. For the application of the present model, β_{M} factors of real pits found on cavities can be evaluated by extracting the model parameters from pit profiles and substituting them into the formula or Fig. 8. The above application allows us to selectively remove pits with large β_{M} factors and might reduce time to cure cavities by local mechanical grinding. The present model is applicable not only to the currently developed niobium cavities, but also to those made of a multilayer superconductor or an alternative material, and even to normal-conducting RF cavities.

Acknowledgements

The work is supported by JSPS Grant-in-Aid for Young Scientists (B), Number 26800157.

Appendix A. Derivation of p_0 and q_0

The map $z = F(w)$ that connects Fig. 5(a) and (b) is given by Eqs. (5) and (13):

$$z = P \int_0^w dw \left(w^2 - 1\right)^{\alpha} w^{-2\alpha} + Q. \tag{A1}$$

B′ on the w-plane is mapped into B on the z-plane. Substituting $z = -iR\tan\pi\alpha$ and $w = 0$ into Eq. (A1), we find $-iR\tan\pi\alpha = q_0 R$, or

$$q_0 = -i\tan\pi\alpha. \tag{A2}$$

Similarly, A′ on the w-plane is mapped into A on the z-plane. Thus, substituting $z = R$ and $w = 1$ into Eq. (A1), we find

$$R = p_0 R \int_0^1 dw \left(w^2 - 1\right)^{\alpha} w^{-2\alpha} - iR\tan\pi\alpha,$$

Downloaded from http://ptep.oxfordjournals.org/ at CERN Library on July 9, 2015

or

$$\frac{1}{\cos\pi\alpha} = p_0 \int_0^1 dw \left(1-w^2\right)^\alpha w^{-2\alpha},$$

where $1 + i\tan\pi\alpha = e^{i\pi\alpha}/\cos\pi\alpha$ and $(w^2-1)^\alpha = e^{i\pi\alpha}(1-w^2)^\alpha$ are used. The integral on the right-hand side can be evaluated by replacing w with $t \equiv w^2$:

$$\begin{aligned}\frac{1}{\cos\pi\alpha} &= \frac{p_0}{2}\int_0^1 dt\,(1-t)^{1+\alpha-1} t^{\frac{1}{2}-\alpha-1} \\ &= \frac{p_0}{2}\frac{\Gamma(1+\alpha)\Gamma\left(\frac{1}{2}-\alpha\right)}{\Gamma\left(1+\frac{1}{2}\right)} \\ &= p_0 \frac{\alpha\Gamma(\alpha)\Gamma\left(\frac{1}{2}-\alpha\right)}{\sqrt{\pi}}.\end{aligned}$$

Then we obtain

$$p_0 = \frac{\sqrt{\pi}}{\alpha\cos\pi\alpha\,\Gamma(\alpha)\Gamma\left(\frac{1}{2}-\alpha\right)}. \tag{A3}$$

Appendix B. Derivation of p, q, and Δ

The map $z = F(w)$ that connects Fig. 6(a) and (b) is given by Eqs. (5), (21), and (22):

$$z(w) = pR\int_0^w dw\left(w^2-w_n^2\right)^{\frac{\alpha}{2n}}\left(w^2-1\right)^{\frac{\alpha}{2n}} w^{-2\alpha}\prod_{k=1}^{n-1}\left(w^2-w_k^2\right)^{\frac{\alpha}{n}} + qR. \tag{B1}$$

B$'$ on the w-plane is mapped into B on the z-plane. Thus, substituting $z = -iR\tan\pi\alpha$ and $w = 0$ into Eq. (B1), we find $-iR\tan\pi\alpha = qR$, or

$$q = -i\tan\pi\alpha. \tag{B2}$$

A_1' on the w-plane is mapped into A_1 on the z-plane. Substituting $w = w_1$ into Eq. (B1), we find

$$z(w_1) = pR\int_0^{w_1} dw f_n(w) + qR = z(1) + pR\int_1^{w_1} dw f_n(w).$$

Since $z(w_1) - z(1) = 2r_e\sin(\pi\alpha/2n)e^{i\left(\pi\alpha-\frac{\pi\alpha}{2n}\right)}$, we obtain

$$2\frac{r_e}{R}\sin\frac{\pi\alpha}{2n} = p\int_1^{w_1} dw\left(w_n^2-w^2\right)^{\frac{\alpha}{2n}}\left(w^2-1\right)^{\frac{\alpha}{2n}} w^{-2\alpha}\prod_{k=1}^{n-1}\left(w_k^2-w^2\right)^{\frac{\alpha}{n}}. \tag{B3}$$

When $\Delta \ll 1$, the above integral can be performed. Substituting Eq. (22) and $w = 1+\xi$ ($|\xi| \ll 1$) into Eq. (B3), we obtain

$$\begin{aligned}2\frac{r_e}{R}\sin\frac{\pi\alpha}{2n} = p\,2^\alpha \int_0^{\frac{2\Delta}{n-2}} d\xi \left(\frac{n+2}{n-2}\Delta-\xi\right)^{\frac{\alpha}{2n}} \xi^{\frac{\alpha}{2n}}(1+\xi)^{-2\alpha} \\ \times\left(\frac{2\Delta}{n-2}-\xi\right)^{\frac{\alpha}{n}}\prod_{k=2}^{n-1}\left(\frac{k+1}{n-2}\Delta-\xi\right)^{\frac{\alpha}{n}}\end{aligned}$$

Downloaded from http://ptep.oxfordjournals.org/ at CERN Library on July 9, 2015

$$\simeq p\,2^{\alpha}\left(\frac{1}{2}\frac{2\Delta}{n-2}\right)\left[\left(\frac{n+2}{n-2}\Delta-\xi\right)^{\frac{\alpha}{2n}}\xi^{\frac{\alpha}{2n}}(1+\xi)^{-2\alpha}\right.$$
$$\left.\times\left(\frac{2\Delta}{n-2}-\xi\right)^{\frac{\alpha}{n}}\prod_{k=2}^{n-1}\left(\frac{k+1}{n-2}\Delta-\xi\right)^{\frac{\alpha}{n}}\right]\Bigg|_{\frac{1}{2}\frac{2\Delta}{n-2}}$$
$$=p\,2^{\alpha}\left(\frac{\Delta}{n-2}\right)^{1+\alpha}(n+1)^{\frac{\alpha}{2n}}\left(1+\frac{\Delta}{n-2}\right)^{-2\alpha}\Gamma(n)^{\frac{\alpha}{n}},$$

where $\prod_{k=2}^{n-1}k=(n-1)!=\Gamma(n)$ is used. At $n\to\infty$, this equation is reduced to

$$\frac{r_e}{R}\pi\alpha=p\,2^{\alpha}\Delta^{1+\alpha}e^{-\alpha}, \tag{B4}$$

where $\Gamma(n)^{\frac{1}{n}}/n\to e^{-1}$ is used.

A_0' on the w-plane is mapped into A_0 on the z-plane. Substituting $z=[R\tan\pi\alpha-r_e(1-\cos\pi\alpha)]/\tan\pi\alpha-ir_e(1-\cos\pi\alpha)$ and $w=1$ into Eq. (B1), we find

$$\frac{R\tan\pi\alpha-r_e(1-\cos\pi\alpha)}{\tan\pi\alpha}-ir_e(1-\cos\pi\alpha)=pR\int_0^1 dw f_n(w)-iR\tan\pi\alpha,$$

or

$$\frac{R\tan\pi\alpha-r_e(1-\cos\pi\alpha)}{R\sin\pi\alpha}=p\int_0^1 dw\left(w_n^2-w^2\right)^{\frac{\alpha}{2n}}\left(1-w^2\right)^{\frac{\alpha}{2n}}w^{-2\alpha}\prod_{k=1}^{n-1}\left(w_k^2-w^2\right)^{\frac{\alpha}{n}}. \tag{B5}$$

When $\Delta\ll 1$, w_k $(k=1,\ldots,n)$ can be approximated by $1+w_n/2=1+\Delta/2$. Thus, Eq. (B5) becomes

$$\frac{1}{\cos\pi\alpha}-\frac{r_e}{R}\frac{1-\cos\pi\alpha}{\sin\pi\alpha}\simeq p\int_0^1 dw\left[\left(1+\frac{\Delta}{2}\right)^2-w^2\right]^{\alpha}w^{-2\alpha}$$
$$=\frac{p}{2}\left(1+\frac{\Delta}{2}\right)^{2\alpha}\int_0^1 dt(1-\zeta t)^{\alpha}t^{-\alpha+\frac{1}{2}-1}(1-t)^0$$
$$=\frac{p}{2}\left(1+\frac{\Delta}{2}\right)^{2\alpha}\frac{\Gamma(b)\Gamma(c-b)}{\Gamma(c)}\,{}_2F_1(a,b;c;\zeta),$$

where $a=-\alpha$, $b=-\alpha+\frac{1}{2}$, $c=1+b$, $\zeta=(1+\Delta/2)^{-2}\simeq(1-\Delta)$, and ${}_2F_1(a,b;c;\zeta)$ is the Gaussian hypergeometric function. By using the relations $\Gamma(c-b)=\Gamma(1)=1$ and $\Gamma(c)=\Gamma(1+b)=b\Gamma(b)$, the condition is further simplified:

$$\frac{1}{\cos\pi\alpha}-\frac{r_e}{R}\frac{1-\cos\pi\alpha}{\sin\pi\alpha}=p\frac{1+\alpha\Delta}{1-2\alpha}\,{}_2F_1(a,b;c;\zeta). \tag{B6}$$

Appendix C. Derivation of Eq. (26)

Substituting $w=w_{\rm M}\equiv(1+w_n)/2$ into

$$f_n(w)=\left(w^2-w_n^2\right)^{\frac{\alpha}{2n}}\left(w^2-1\right)^{\frac{\alpha}{2n}}w^{-2\alpha}\prod_{k=1}^{n-1}\left(w^2-w_k^2\right)^{\frac{\alpha}{n}},$$

with the assumption $\Delta\ll 1$, we obtain

$$f_n(w_{\rm M})\simeq 2^{\alpha}(-1)^{\frac{\alpha}{2n}}\left(\frac{\Delta}{n-2}\right)^{\alpha}\left(1+\frac{n}{2}\right)^{\frac{\alpha}{n}}\frac{\prod_{k=0}^{n}\left(\frac{n}{2}-k\right)^{\frac{\alpha}{n}}}{\left(\frac{n}{2}\right)^{\frac{\alpha}{n}}\left(-\frac{n}{2}\right)^{\frac{\alpha}{n}}}.$$

Downloaded from http://ptep.oxfordjournals.org/ at CERN Library on July 9, 2015

Then, at $n \to \infty$, we obtain

$$\lim_{n\to\infty} |f_n(w_{\rm M})| = 2^\alpha \lim_{n\to\infty} \left(\frac{\Delta}{n-2}\right)^\alpha \left|\prod_{k=0}^{n} \left(\frac{n}{2}-k\right)^{\frac{\alpha}{n}}\right|.$$

By using the relation

$$\left|\prod_{k=0}^{n}\left(\frac{n}{2}-k\right)\right| = \left|\frac{n}{2}\cdot\frac{n-2}{2}\cdots\frac{1}{2}\cdot\frac{-1}{2}\cdot\frac{-3}{2}\cdots\frac{-(n-2)}{2}\cdot\frac{-n}{2}\right| = \prod_{k=0}^{\frac{n-1}{2}}\left(\frac{1}{2}+k\right)^2,$$

and the definition of the Gamma function in the infinite-product form,

$$\Gamma(1/2) = \lim_{m\to\infty} \frac{m^{\frac{1}{2}} m!}{\prod_{k=0}^{m}\left(\frac{1}{2}+k\right)},$$

we find $\lim_{n\to\infty} |f_n(w_{\rm M})| = e^{-\alpha}\Delta^\alpha$ and thus

$$\beta_{\rm M} \simeq \lim_{n\to\infty}\left|\frac{1}{f_n(w_{\rm M})}\right| = e^\alpha \Delta^{-\alpha}. \tag{C1}$$

References

[1] H. Padamsee, J. Knobloch, and T. Hays, *RF Superconductivity for Accelerators* (John Wiley, New York, 1998).
[2] G. Ciovati, Proc. IPAC2013, Shanghai, China, p. 3124, THYB201 (2013).
[3] W. Singer et al., Phys. Rev. ST Accel. Beams **16**, 012003 (2013).
[4] A. Gurevich, Rev. Accel. Sci. Technol. **5**, 119 (2012).
[5] K. Saito et al., Proc. SRF1989, KEK, Tsukuba, Japan, p. 635, SRF89G18 (1989).
[6] T. Furuya, Proc. SRF1989, KEK, Tsukuba, Japan, p. 305, SRF89D02 (1989).
[7] Ph. Bernard, D. Bloess, T. Flynn, C. Hauviller, W. Weingarten, P. Bosland, and J. Martignac, Proc. EPAC1992, Berlin, Germany, p. 1269 (1992).
[8] K. Saito, H. Miwa, K. Kurosawa, P. Kneisel, S. Noguchi, E. Kako, M. Ono, T. Shishido, and T. Suzuki, Proc. SRF1993, CEBAF, Newport Mews, Virginia, USA, p. 1151, SRF93J03 (1993).
[9] P. Kneisel, B. Lewis, and L. Turlington, Proc. SRF1993, CEBAF, Newport Mews, Virginia, USA, p. 628, SRF93I09 (1993).
[10] Y. Kojima, et al., Proc. SRF1989, KEK, Tsukuba, Japan, p. 85, SRF89A07 (1989).
[11] Y. Iwashita, Y. Tajima, and H. Hayano, Phys. Rev. ST Accel. Beams **11**, 093501 (2008).
[12] M. S. Champion, L. D. Cooley, C. M. Ginsburg, D. A. Sergatskov, R. L. Geng, H. Hayano, Y. Iwashita, and Y. Tajima, IEEE Trans. Appl. Supercond. **19**, 3 (2009).
[13] Y. Yamamoto, Nucl. Instrum. Methods Phys. Res. A **623**, 579 (2010).
[14] M. Ge, G. Wu, D. Burk, J. Ozelis, E. Harms, D. Sergatskov, D. Hicks, and L. D. Cooley, Supercond. Sci. Technol. **24**, 035002 (2011).
[15] Y. Yamamoto, H. Hayano, E. Kako, S. Noguchi, T. Shishido, and K. Watanabe, Nucl. Instrum. Methods Phys. Res. A **729**, 589 (2013).
[16] J. Knobloch, R. L. Geng, M. Liepe, and H. Padamsee, Proc. SRF1999, La Fonda Hotel, Santa Fe, New Mexico, USA, p. 77, TUA004 (1999).
[17] Y. Iwashita, and T. Higo, Proc. LINAC 2004, Lübeck, Germany, p. 501, TUP95 (2004).
[18] S. Berry, C. Antoine, and M. Desmons, Proc. EPAC2004, Lucerne, Switzerland, p. 1000 (2004).
[19] V. Shemelin, and H. Padamsee, TTC Report SRF 080903-04 (2008).
[20] Y. Morozumi, Proc. IPAC'10, Kyoto, Japan, p. 2932, WEPEC020 (2010).
[21] Y. Xie, M. Liepe, and H. Padamsee, Proc. SRF2011, Chicago, IL, USA, p. 687, THPO001 (2011).
[22] Y. Xie, and M. Liepe, Proc. SRF2013, Paris, France, p. 378, TUIOA05 (2013).
[23] R. Schinzinger, and P. A. A. Laura, *Conformal Mapping: Methods and Applications* (Dover Publications, Inc., New York, 2003).
[24] R. Miller, Y. Y. Lau, and J. H. Booske, Appl. Phys. Lett. **91**, 074105 (2007).
[25] R. Miller, Y. Y. Lau, and J. H. Booske, J. Appl. Phys. **106**, 104903 (2009).

Downloaded from http://ptep.oxfordjournals.org/ at CERN Library on July 9, 2015

[26] K. Halbach, and R. F. Holsinger, Particle Accelerators **7**, 213 (1976).
[27] Reference Manual for the POISSON/SUPERFISH Group of Codes, Los Alamos National Laboratory Report LA-UR-87-126 (1987).
[28] User's Guide for the POISSON/SUPERFISH Group of Codes, Los Alamos National Laboratory Report LA-UR-87-115 (1987).
[29] T. Kubo, Proc. SRF2013, Paris, France, p. 433, TUPO008 (2013).
[30] T. Kubo, Proc. IPAC'14, Dresden, Germany, p. 2525, WEPRI024 (2014).
[31] K. Watanabe, Proc. SRF2009, Berlin, Germany, p. 123, TUOBAU01 (2009).
[32] K. Watanabe, H. Hayano, and Y. Iwashita, Proc. SRF2011, Chicago, IL, USA, p. 598, WEIOB02 (2011).
[33] Y. Yamamoto, H. Hayano, E. Kako, S. Noguchi, T. Shishido, and K. Watanabe, Proc. IPAC2012, New Orleans, Louisiana, USA, p. 2233, WEPPC013 (2012).
[34] A. Gurevich, Appl. Phys. Lett. **88**, 012511 (2006).
[35] T. Kubo, Y. Iwashita, and T. Saeki, Appl. Phys. Lett. **104**, 032603 (2014).
[36] S. Posen, M. Liepe, and D. L. Hall, Appl. Phys. Lett. **106**, 082601 (2015).
[37] T. Kubo, Prog. Theor. Exp. Phys. **2015**, 063G01 (2015).

Downloaded from http://ptep.oxfordjournals.org/ at CERN Library on July 9, 2015